RSC Advances

ROYAL SOCIETY OF CHEMISTRY

PAPER

View Article Online
View Journal | View Issue

Check for updates

Cite this: *RSC Adv.*, 2018, **8**, 28625

Coherent nanoscale cobalt/cobalt oxide heterostructures embedded in porous carbon for the oxygen reduction reaction†

Xue-Cheng Li,[a] Fa-Shuang She,[a] Dong Shen,[c] Chao-Ping Liu,[d] Li-Hua Chen,[a] Yu Li,[a] Zhao Deng,*[a] Zhen-Hua Chen*[b] and Hong-En Wang*[a]

Received 18th May 2018
Accepted 6th August 2018

DOI: 10.1039/c8ra04256j

rsc.li/rsc-advances

Cost-effective and efficient electrocatalysts for the oxygen reduction reaction (ORR) are crucial for fuel cells and metal–air batteries. Herein, we report the facile synthesis of a $Co/CoO/Co_3O_4$ heterostructure embedded in a porous carbon matrix by refluxing and annealing. This composite exhibits several structural merits for catalyzing the ORR: (1) the existence of metallic Co and graphitic carbon enhanced the electrical conduction; (2) the porous, loose carbon network facilitated the electrolyte permeation and mass transport; (3) more importantly, the nanosized coherent CoO/Co_3O_4 heterojunctions with structural defects and oxygen vacancies enhanced the charge transport/separation at the interface and adsorption affinity to O_2, thus promoting the ORR kinetics and lowering the reaction barrier. Consequently, the composite electrode manifests high electrocatalytic activity, attaining a current density of 6.7 mA cm^{-2} at −0.8 V (*vs.* Ag/AgCl), which is superior to pure CoO nanoparticles (4.7 mA cm^{-2}), and has good methanol tolerance. The present strategy based on heterostructure and vacancy engineering may pave the way for the exploration of more advanced, low-cost electrocatalysts for electrochemical reduction and evolution processes.

Introduction

Exploring new electrocatalyst materials to enhance the sluggish oxygen reduction reaction (ORR) kinetics is key to various renewable energy conversion and storage applications such as fuel cells and rechargeable metal–air batteries.[1] Pt- and Pd-based materials have been considered the most efficient electrocatalysts for the ORR so far due to their high activity.[2–7] However, the high cost, scarcity and poor stability/durability of Pt have hindered its widespread applications. Various non-precious metal catalysts with comparable catalytic activity and high durability have been extensively sought to substitute Pt in recent years.[8–16] Among them, cobalt-based materials (Co,[17,18] Co_3O_4,[19–21] CoO[22] and their composites[23–27]) have been intensively studied as promising alternatives to Pt-based electrocatalysts for the ORR due to their tunable composition, morphology, microstructures and rich active sites. Nonetheless, Co-based nanomaterials still have some disadvantages, such as easy aggregation and low electronic conductivity, leading to decreased active surface area and poor charge transfer/transport kinetics during electrochemical redox reactions. Encapsulating Co or cobalt oxides into porous carbon frameworks can in principle boost the electrical conduction and form strong interfacial electron coupling, resulting in enhanced electrocatalytic activity and stability.[28,29] In addition, intentional and rational design and fabrication of Co/CoO_x heterojunctions could potentially further improve the interfacial charge transfer and electron transport, featuring better electrocatalytic property than single Co/CoO_x components.[30–32] However, the effective synthesis of such composite materials that can combine all structural advantages remains challenging and deserves further study.

In this paper, we report the designed synthesis of $Co/CoO/Co_3O_4$ heterostructure (denoted as CoO_x) embedded in porous carbon matrix as efficient catalyst for ORR. The composite was obtained by a simple refluxing followed by annealing treatment. The synergic coupling of coherent CoO/Co_3O_4 heterojunctions and presence of metallic Co and conductive amorphous carbon enable the material a high and stable electrocatalytic performance. Our work presented herein can provide new insights into the rational design and synthesis of new heterostructure-type transition metal compounds for electrochemical energy conversion and storage applications.

---

[a] *State Key Laboratory of Advanced Technology for Materials Synthesis and Processing, Wuhan University of Technology, 122 Luoshi Road, Hongshan District, Wuhan 430070, China. E-mail: dengzhao@whut.edu.cn; hongenwang@whut.edu.cn*

[b] *Shanghai Synchrotron Radiation Facility (SSRF), Shanghai Institute of Applied Physics, Chinese Academy of Sciences, Shanghai 201800, China. E-mail: chenzhenhua@sinap.ac.cn*

[c] *Department of Chemistry and Center of Diamond and Advanced Films (COSDAF), City University of Hong Kong, HKSAR, China*

[d] *Department of Physics, City University of Hong Kong, HKSAR, China*

† Electronic supplementary information (ESI) available. See DOI: 10.1039/c8ra04256j

Experimental section

All the chemicals were of analytical pure grade and used as received without further purification.

Material synthesis

Synthesis of CoO nanoparticles

Pure CoO nanoparticles were prepared by a mild refluxing process in oleylamine under Ar protection referring our previous work[33] with little modifications. In a typical procedure, a mixture of Co(acetylacetonate)$_3$ (1.6 mmol) and oleylamine (80 mmol) was heated to 135 °C and maintained at this temperature for 90 min with magnetic stirring. The resulting solution was then heated to 200 °C within 5 min and refluxed at this temperature for another 60 min, finally cooled to room temperature naturally. During this process, the Co(acetylacetonate)$_3$ was decomposed into nanosized CoO *in situ* capped with oleylamine. After reaction, excess ethanol was added to the resulting mixture to precipitate the brown product. The resultant CoO nanoparticles were thoroughly washed with ethanol to remove the residual oleylamine adsorbed on their surface, and were dried under Ar protection before being dispersed in hexane again for further use.

Synthesis of CoO$_x$/C composite

CoO$_x$/C composite sample was prepared by annealing the refluxed CoO product before removing oleylamine (without rinsing) in a tube furnace at setting temperatures (400–800 °C) for 2 h under purged Ar. For simplicity, the samples obtained after thermal treatment at 400 °C, 600 °C and 800 °C were donated as CoO$_x$-400, CoO$_x$-600 and CoO$_x$-800, respectively.

Characterizations

X-ray diffraction (XRD) patterns were recorded on a Bruker diffractometer with Cu Kα radiation (λ = 1.54056 Å) at 40 kV mA^{-1}. The morphology of the samples was observed by a scanning electron microscope (SEM, Hitachi S-4800) equipped with an energy-dispersive X-ray (EDX) analyzer. Transmission electron microscopy (TEM) and high-resolution TEM (HRTEM) micrographs were acquired on a JEOL JEM-2100F microscope at 200 kV. Raman measurement was performed at room temperature by an Invia Raman microscope (Renishaw, UK) using 633 nm excitation wavelength. The electronic states and surface composition of the sample were analyzed by X-ray photoelectron spectroscope (XPS, Thermo fisher, Alpha). The binding energies (BE) for the sample were calibrated using C 1s peak from a carbon tape at 284.8 eV.

Electrochemical tests

Electrochemical measurements were recorded on a CHI 660D electrochemical workstation in a three-electrode system at room temperature. The glassy carbon electrode with a diameter of 5 mm, Pt foil and Ag/AgCl were used as working electrode, counter electrode and reference electrode, respectively. The electrochemical experiments were carried out in an O$_2$-saturated 0.1 M KOH aqueous solution electrolyte. To prepare the working electrode, 5 mg sample and 15 μL Nafion solution (5 wt%) was thoroughly dispersed in 1 mL water and isopropanol (volume ratio of 3 : 1) by sonication for 30 min to form a homogeneous ink. Then 4 μL of catalyst ink (containing ~20 μg catalyst) was cast on the surface of the glassy carbon electrode and dried in air. The rotating-disk electrode (RDE) measurements were carried out at a sweep rate of 5 mV s^{-1} with varied rotation speeds from 400 to 2025 rpm. To evaluate the methanol resistance capability of the electrode, cyclic voltammetry (CV) sweep was recorded in an O$_2$-saturated 0.1 M KOH electrolyte with and without addition of 3 M methanol for comparison.

Results and discussion

The crystal structure of the as-prepared samples was first studied by XRD analysis. As shown in Fig. 1, the crystallinity of the samples increases along with the increase of annealing temperature as reflected by sharp diffraction peaks. All the three samples contain cubic CoO (space group $Fm3m$, JCPDS 01-1227)[30] and cubic metallic Co (space group $Fm3m$, JCPDS 15-0806),[17] suggesting the CoO can be easily reduced to Co species by surface residual oleylamine under inert atmosphere. In addition, two additional peaks (marked by "*" and "#") are noted in CoO$_x$-600 and cannot be indexed to known cobalt-based compounds, which may be related to the formation of some unknown intermediate products. Another interesting feature is that cubic Co$_3$O$_4$ (space group $Fd3m$, JCPDS 01-1152)[20a] can also exist in the CoO$_x$-800 and CoO$_x$-600 sample because at high annealing temperatures some exposed Co species formed by the removal of most adjacent carbon species (in form of CO or CO$_2$) may be re-oxidized into Co$_3$O$_4$.[20b] However, from Fig. 1 the strong diffraction peak of (311) plane (red) for Co$_3$O$_4$ at $2\theta = \sim 37°$ (Note that it may also be (111) plane (black) for CoO) has a much weaker intensity compared to the strong diffraction peak of (111) plane (blue) for Co, suggesting the low content of Co$_3$O$_4$ (CoO) relative to Co species in the

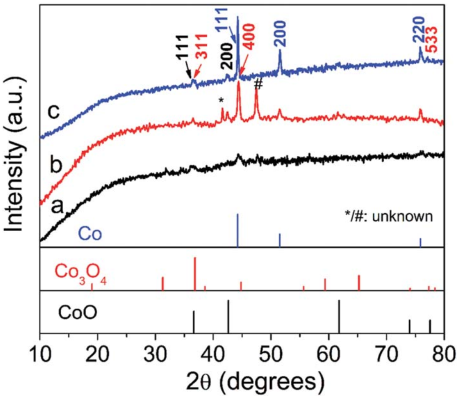

Fig. 1 XRD patterns of (a) CoO$_x$-400, (b) CoO$_x$-600 and (c) CoO$_x$-800 samples.

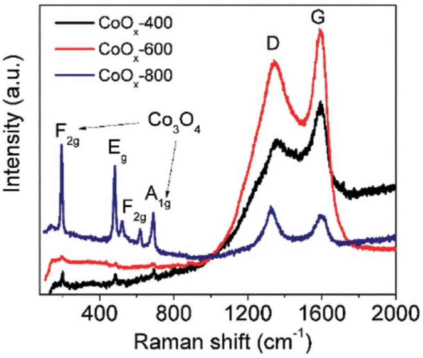

Fig. 2 Raman spectra of the samples prepared by refluxing and annealing for 2 h in Ar at 400 °C (CoO$_x$-400), 600 °C (CoO$_x$-600) and 800 °C (CoO$_x$-800).

composite. However, the low content of Co_3O_4 and the superimposition of major diffraction peaks position between Co_3O_4 and CoO make the identification of Co_3O_4 difficult and challenging. For this, its presence has been further confirmed by the existence of Co^{3+} species in XPS and HRTEM analyses in the following.

The crystal and carbon structure of the CoO$_x$ was further analyzed by Raman spectra, as shown in Fig. 2. The noticeable peaks can be indexed to the F_{2g} (196.5 cm^{-1}), E_g (480.9 cm^{-1}), F_{2g} (517.7 and 617.7 cm^{-1}) and A_{1g} (686.2 cm^{-1}) modes of Co_3O_4,[34] further evidencing the existence of Co_3O_4 phase localized mainly at surface. Compared to literature,[34] all the Raman peaks for Co_3O_4 in the composite shifted to lower wavenumbers possibly caused by the presence of oxygen vacancies[35,36] as further discussed in the XPS analyses in the following. Another two strong Raman peaks centering around 1357 cm^{-1} and 1605 cm^{-1} can be assigned to the D-band (vibrations of sp^3-hybridized carbon atoms with dangling bonds) and G-band (sp^2-bonded carbon atoms) of graphitic carbon, respectively,[37,38] formed by carbonization of residual oleylamine. It is found that the intensity of D and G bands of the products increased first with increasing temperature, while it decreased with further increasing temperature. Generally, the D and G bands represent the degree of graphitization and content of the graphitized carbon in the composite. Therefore, the enhancement of D and G band intensity of CoO$_x$-600 relative to CoO$_x$-400 can signify an increase of the graphitized carbon in the composite because the annealing temperature of 400 °C is still low for carbonization process. This can also be reflected in the following SEM characterization, which reveals that the morphology of CoO$_x$-400 doesn't alter much compared to CoO. Instead, the CoO$_x$-600 product contains some 1D nanostructures (probably carbon nanotubes) that are formed by carbonization catalyzed by the metallic Co species. However, further increasing annealing temperature to 800 °C, the carbon species can further reduce CoO into Co; meantime, some carbon substances are converted into CO or CO_2 and thus consumed, giving rise to reduced total graphitized carbon in the composite and a lowered D and G band intensity in Raman as well. In addition, the slight increase of intensity for I_D relative to I_G in CoO$_x$-800 compared to CoO$_x$-400 and CoO$_x$-600 can be mainly ascribed to the possible presence of some strain at the Co/CoO/Co_3O_4 and carbon interface in the composite as revealed by the fusion of most nanoparticles together in the CoO$_x$-800 product from SEM observation.

The surface valence electronic states and element composition in the CoO$_x$-800 sample were investigated by XPS. The survey XPS spectrum in Fig. 3a validates the existence of Co, O and C elements in the sample. The deconvolution of Co 2p core level XPS reveals the presence of three pairs of peaks (Fig. 3b). The first pair of peaks with lower binding energies (BE) centered at 779.4 eV and 794.4 eV can be ascribed to Co $2p_{3/2}$ and Co $2p_{1/2}$ of metallic Co.[26] Another pair of peaks with BE at 780.4 and 795.9 eV can be assigned to the $2p_{3/2}$ and $2p_{1/2}$ of Co^{3+} in Co_3O_4.[20] The two bands at higher BE of 781.8 and 797.3 eV correspond to the $2p_{3/2}$ and $2p_{1/2}$ of Co^{2+} in CoO/Co_3O_4.[20,39] Additionally, two broad bands centering at 784 eV and 803 eV are noted for shakeup satellite peaks of Co^{2+} and Co^{3+}.[39] A rough estimation from the area ratio of Co^{3+} (for Co_3O_4) to Co^0 in metallic Co species reveals the content of Co_3O_4 is comparable to that of Co on the surface. This result does not violate the XRD result because XPS is a surface-sensitive characterization. On the contrary, these XPS data further support that the Co_3O_4 species mainly localize on the composite surface and prevent further oxidation of Co underneath. Fig. 3c depicts the O 1s XPS spectrum, which can be deconvoluted into three bands: O–Co bond (529.6 eV),[39] oxygen vacancy (V_o, 531 eV),[35] and O–C bond (532.1 eV).[40] Note that the V_o can be ascribed to the incomplete reduction from CoO to Co during carbonization of organics. The deconvolution of C 1s spectrum in Fig. 3d indicates the presence of C–C/C=C bonds for graphite carbon (284.4 eV), C–O bond (285.8 eV) and C=O bond (288 eV) for surface functional groups.[40,41]

The surface morphologies of the prepared CoO$_x$ samples were first observed by SEM. In Fig. 4a, the CoO sample synthesized by refluxing alone contains spherical nanoparticles with sizes of 20–30 nm, which is in consistent with previous work.[33] After annealing the refluxed CoO at 400 °C for 2 h in Ar, the resultant sample (CoO$_x$-400) is composed of some larger particles with sizes of 40–60 nm that are fused together (Fig. 4b). In CoO$_x$-600 sample, some large aggregates (~400 nm) and copious 1D carbon nanostructures are observed (marked by white arrows). The formation of such 1D carbon nanomaterials can be probably due to the catalytic effect of Co species. That is, metallic Co formed during the carbonized process in turn catalyzed the production of 1D nanostructured carbon.[42] For the CoO$_x$-800 sample, it mainly comprises larger aggregates with few 1D carbon nanostructures (Fig. 4d). The formation of such aggregates suggests the fusion of most CoO$_x$ particles mediated by carbon species to minimize the total surface energy of the whole system during annealing process. Fig. 5 shows the SEM micrograph of the CoO$_x$-800 sample and corresponding EDX map of C, O and Co elements, proving their relatively uniform distribution.

Fig. 6 presents the TEM and HRTEM micrographs of the CoO$_x$-800 sample. The TEM in Fig. 6a shows several CoO$_x$ particles with sizes of ~100 nm that are embedded in a porous carbon matrix. In addition, few CoO$_x$ particles have exposed

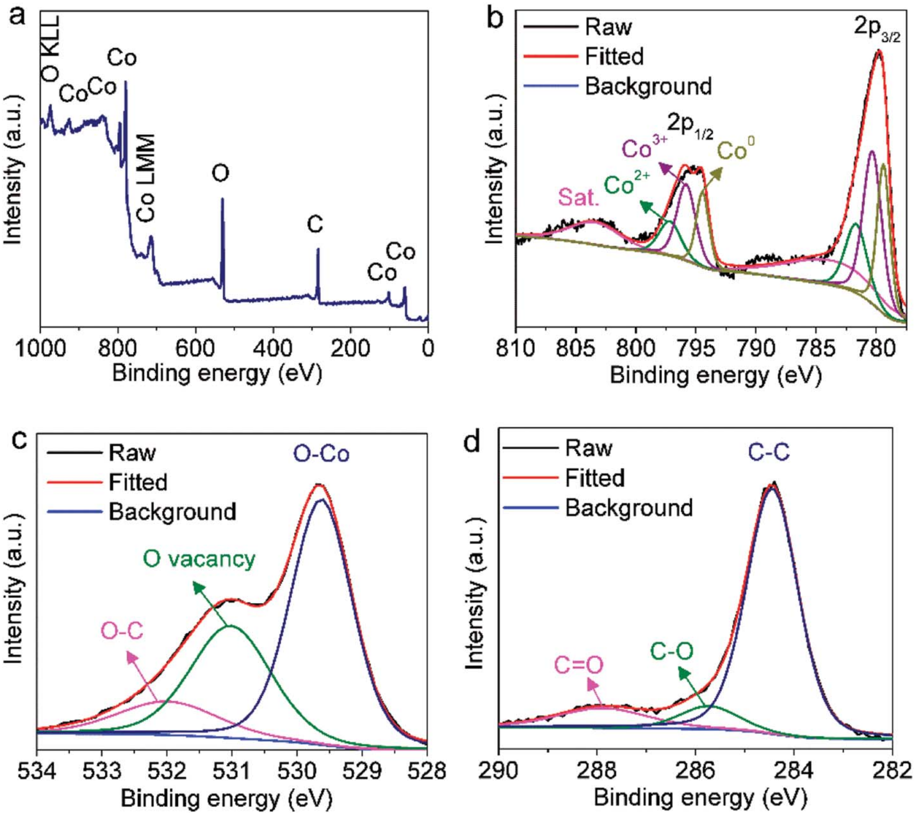

Fig. 3 (a) XPS survey spectrum and high-resolution XPS spectra of (b) Co 2p, (c) O 1s and (d) C 1s core levels in CoO_x-800 sample.

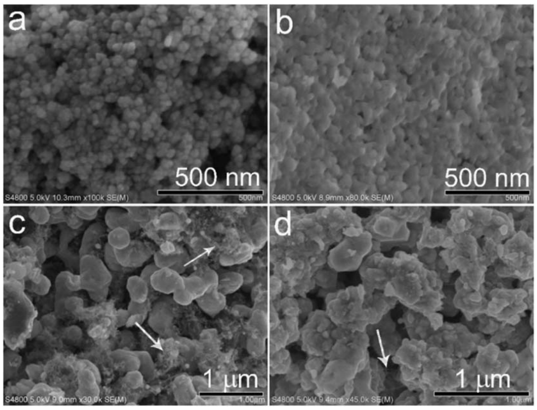

Fig. 4 SEM images of the samples synthesized by refluxing (a), and annealing in Ar at 400 °C (CoO_x-400) (b), 600 °C (CoO_x-600) (c) and 800 °C (CoO_x-800) (d), respectively.

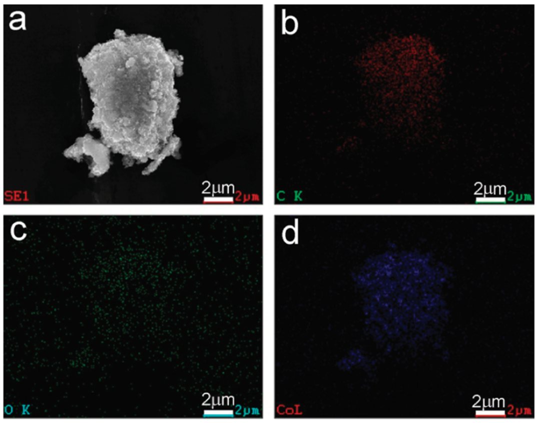

Fig. 5 (a) SEM image and EDX mappings of (b) C, (c) O, and (d) Co elements in the CoO_x-800 sample, evidencing their relatively uniform distribution.

surface (without coating with carbon layer) possibly due to the complete removal of organics surrounding them. In Fig. 6b, some ring-like carbon nanostructures are observed as indicated by black arrows. The formation of such carbon nanostructure can be ascribed to the carbonization of organics into carbon nanotubes catalyzed by Co species, which agrees with the SEM result (Fig. 4d). Fig. 6c displays the HRTEM micrograph of a portion of a single CoO_x particle capped by thin carbon layers (~5 nm thick as marked by black arrows). Fast Fourier Transform (FFT) image in Fig. 6d taken from area 1 in Fig. 6c (marked by white square at the bottom left) clearly reveals the coexistence of cubic CoO (JCPDS 01-1227) and Co_3O_4 (JCPDS 01-1152) phases, suggesting the formation of nanoscale coherent CoO/Co_3O_4 heterojunctions in the composite. The inverse FFT (IFFT) image in Fig. 6e obtained from (111) and (11−1) planes in Fig. 6d (labelled by yellow color) after applying a filter depicts a 2D lattice image of CoO with some distortions, suggesting the presence of some defects (*e.g.*, edge dislocations and oxygen vacancy).[35] The HRTEM image of the area 2 in Fig. 6c (white square on the top right) and corresponding FFT image (Fig. 6f) further confirm the coexistence of CoO/Co_3O_4 phases with a sharp interface (marked by the black dotted line in Fig. 6c). Note that both domains 1 and 2 in Fig. 6c contain Co_3O_4 phase. Careful inspection indicates that these two domains are both located at the (thin) edge regions with incomplete carbon encapsulation, meaning that Co_3O_4 can be formed by the re-oxidation of the exposed Co species upon exposure to air.

Based on the above characterizations, we deduce that during the carbonization process some newly formed Co species can migrate, fuse and segregate together with exposed surface accompanied by the removal of some carbonaceous substances (CO, CO_2 *etc.*). The exposed Co surface can then be easily re-oxidized into Co_3O_4 upon exposure to air. Once oxidation, the newly formed Co_3O_4 layer as well as the carbon encapsulation can prevent the complete oxidation of all Co species. Therefore, a composite of CoO/Co/Co_3O_4 with carbon was produced in the end.

It should be stressed that the finding of coexistence of Co_3O_4 at surface due to spontaneous oxidation of Co is important for catalysis-related research because most of these reactions are surface-involved/sensitive process involving O_2. Therefore, the surface composition, (micro) structure and chemical states of Co and Co-based compounds will undoubted exert a crucial role on the catalytic property of this class of electrocatalyst materials.

Fig. 7a shows the ORR polarization curves of CoO, CoO_x-400, CoO_x-600 and CoO_x-800 obtained at a rotation rate of 1600 rpm in an O_2-saturated 0.1 M KOH electrolyte. It is clear that CoO_x-800 electrode exhibits a higher current of 6.7 mA cm^{-2} at −0.8 V, which is superior to that of CoO (4.7 mA cm^{-2}), CoO_x-400 (5.9 mA cm^{-2}), and CoO_x-600 (6.2 mA cm^{-2}) electrodes as well as the electrodes comprised of commercial Co_3O_4 (2.25 mA cm^{-2}) and CoO (1.8 mA cm^{-2}) nanoparticles (Fig. S1†) at the same applied potential. Besides, CoO_x-800 sample shows a halfwave potential of *ca.* −0.28 V (*vs.* Ag/AgCl), which is 50 mV more positive than that of pristine CoO (−0.33 V). These results suggest that the CoO_x-800 material exhibits better electrocatalytic activity toward ORR process. Note that our CoO_x-800 electrode also exhibits better or comparable electrocatalytic activity to that of some other Co-based compounds in previous literatures, such as Co/CoO nanoparticles assembled on graphene,[23] Co/CoO nanoparticles immobilized on Co–N doped carbon,[25] Co–N–C framework,[43] and N-doped carbon nanofibers encapsulating Co nanoparticles.[17]

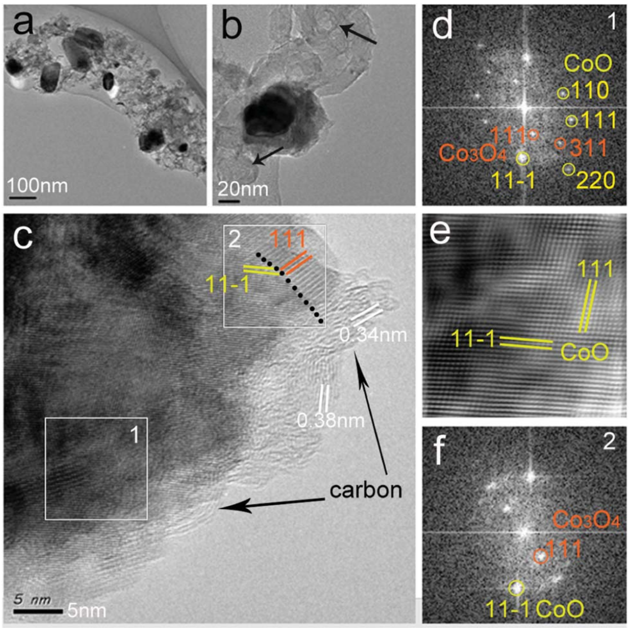

Fig. 6 (a and b) TEM images; (c) HRTEM micrographs; (d and f) fast Fourier transform (FFT) patterns taken from square areas 1 and 2 in (c), respectively; (e) inverse FFT image derived from (111) and (11−1) planes of CoO in (d) of the CoO_x-800 sample.

The reaction kinetics of the CoO_x-800 electrode were further studied by rotating-disk electrode (RDE) voltammetry tests. Linear sweep voltammetry (LSV) profiles in an O_2-saturated 0.1 M KOH electrolyte show that the current response increases with increasing rotation rates from 400 to 2025 rpm (Fig. 7b). The onset potential of CoO_x-800 electrode for the ORR process initiates at *ca.* −0.10 V. The corresponding Koutecky–Levich (K–L) plots in Fig. 7c further exhibit good linearity. The slopes remain approximately constant over the potential range from −0.10 to −0.50 V, suggesting a similar electron-transfer number per O_2 molecule involved in ORR within the scanned potential range. Linearity and parallelism of the plots usually imply first-order reaction kinetics with respect to the concentration of dissolved O_2. The kinetic parameters have been further analyzed using K–L equations following eqn (1)–(3):

$$\frac{1}{J}=\frac{1}{J_\mathrm{L}}+\frac{1}{J_\mathrm{K}}=\frac{1}{B\omega^{1/2}}+\frac{1}{J_\mathrm{K}} \tag{1}$$

$$B=0.62nFC_0D_0^{\,2/3}\nu^{-1/6} \tag{2}$$

$$J_\mathrm{k}=nFkC_0 \tag{3}$$

where J is measured current density, J_K and J_L are kinetic- and diffusion-limiting current densities respectively, ω is angular velocity of the disk ($\omega = 2N\pi$, N is linear rotation speed), n is electron transfer number involved in the reduction of one O_2 molecule, F is Faraday constant (96 485 C mol^{-1}), C_0 is bulk concentration of O_2 dissolved in the electrolyte (1.2×10^{-3} mol L^{-1}), D_0 is diffusion coefficient of O_2 in electrolyte (1.9×10^{-5} cm^2 s^{-1}), ν is kinetic viscosity of the electrode (0.1 m^2 s^{-1}), and k is electron-transfer rate constant. According to eqn (1) and (2), n and J_K can be obtained from the slope and intercept of the K–L plots, respectively.

The average electron transfer numbers of CoO_x-800 sample were calculated to be ∼3.9 at −0.3 to −0.5 V (*vs.* Ag/AgCl), indicating that CoO_x-800 can efficiently catalyze ORR process *via* a four-electron pathway. In addition, the electrochemical stability and methanol tolerance capability are

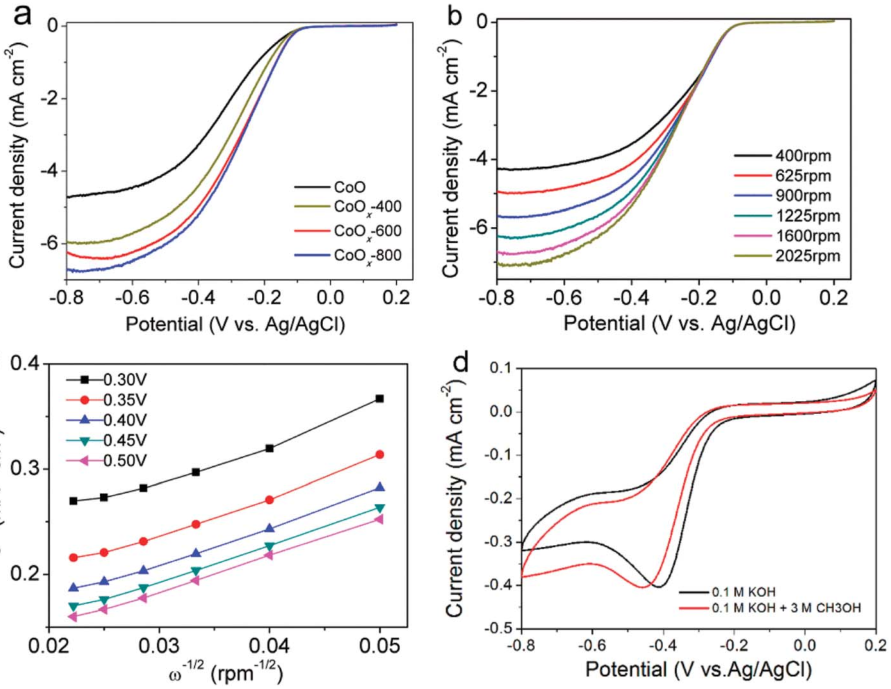

Fig. 7 Electrochemical oxygen reduction on as-prepared CoO_x samples. (a) LSV curves of CoO, CoO_x-400, CoO_x-600 and CoO_x-800 samples with a sweep rate of 5 mV s^{-1} at 1600 rpm; (b) LSV curves of CoO_x-800 electrode at a scan rate of 5 mV s^{-1} under various rotation rates; (c) corresponding Koutecky–Levich plots of CoO_x-800 electrode; (d) CV curves of CoO_x-800 electrodes with (red curve) and without (black curve) adding 3 M methanol into the O_2-saturated 0.1 M KOH electrolyte.

also important performance indicators for ORR electrocatalysts. As seen from Fig. 7d, it is noted that the two curves have comparable peak current (~0.4 mA cm^{-2}) during cathodic process albeit with the more negative potential for the one with addition of methanol, suggesting the addition of methanol only has a slight influence on the ORR process and CoO_x-800 exhibits a relatively robust catalytic capability.

The cycling performance of the CoO_x-800 electrode was further evaluated. As shown in Fig. S2,† the CV curves of the CoO_x-800 electrode in the 1st, 50th, and 1000th cycles almost overlap, suggesting its superior cyclability during the long-term ORR process.

The superior electrocatalytic property of the CoO_x-800 electrode can be mainly attributed to the effective synergy of its unique structural merits in terms of structural defects, phase heterostructure and porous architecture: (1) the presence of metallic Co and graphitic carbon species can significantly enhance the electrical transport within the composite electrode, thus leading to reduced polarization and boosted ORR kinetics; (2) the coherent nanosized CoO/Co_3O_4 heterostructure can further boost the electron transport at interface and propel the O_2 reduction process; (3) the existence of oxygen vacancy (V_o) in CoO can enhance its binding energy towards O_2 and lower the activation energy barrier for O_2 electroreduction; (4) the porous and loose carbon framework can facilitate the electrolyte transport and diffusion of O_2 and reaction intermediates. The synergetic function of the above enables the CoO_x-800 electrode to deliver a superior electrocatalytic performance for ORR process.

Conclusions

In summary, we have demonstrated a facile route for synthesis of a coherent nanoscale $Co/CoO/Co_3O_4$ heterojunction encapsulated in a porous carbon framework. Benefiting from the introduction of graphitized carbon matrix and metallic Co species as well as formation of nanoscale CoO/Co_3O_4 heterostructure with oxygen vacancies, the composite catalyst shows outstanding ORR catalytic activity compared to pure CoO and high methanol tolerance. The present strategy may be extended to the design and fabrication of other heterostructure composite electrocatalysts for electrochemical oxygen reduction and evolution processes.

Conflicts of interest

There are no conflicts to declare.

Acknowledgements

This work is funded by the National Natural Science Foundation of China (Grant No. 51302204). H.-E. Wang thanks the Hubei Provincial Department of Education for the "Chutian Scholar" program. The authors also thank Prof. Bao-Lian Su (University of Namur), Guozhong Cao (University of Washington) and Wenjun Zhang (City University of Hong Kong) for kind support.

References

1 J. L. Liu, D. D. Zhu, C. X. Guo, A. Vasileff and S. Z. Qiao, *Adv. Energy Mater.*, 2017, **7**, 26.

2 Z. X. Yan, H. E. Wang, M. P. Zhang, Z. F. Jiang, T. S. Jiang and J. M. Xie, *Electrochim. Acta*, 2013, **95**, 218–224.

3 Z. X. Yan, M. M. Zhang, J. M. Xie, H. E. Wang and W. Wei, *J. Power Sources*, 2013, **243**, 48–53.

4 J. Ying, J. Li, G. P. Jiang, Z. P. Cano, Z. Ma, C. Zhong, D. Su and Z. W. Chen, *Appl. Catal., B*, 2018, **225**, 496–503.

5 Z. X. Yan, L. N. Gao, C. J. Dai, M. M. Zhang, X. M. Lv and P. K. Shen, *Int. J. Hydrogen Energy*, 2018, **43**, 3705–3715.

6 J. Ying, G. P. Jiang, Z. P. Cano, L. Han, X. Y. Yang and Z. W. Chen, *Nano Energy*, 2017, **40**, 88–94.

7 (*a*) H. Xu, P. P. Song, F. Gao, Y. Shiraishi and Y. K. Du, *Nanoscale*, 2018, **10**, 8246–8252; (*b*) J. B. Ding, L. Z. Bu, S. J. Guo, Z. P. Zhao, E. B. Zhu, Y. Huang and X. Q. Huang, *Nano Lett.*, 2016, **16**, 2762–2767; (*c*) L. Z. Bu, C. Y. Tang, Q. Shao, X. Zhu and X. Q. Huang, *ACS Catal.*, 2018, **8**, 4569–4575.

8 H. Xu, B. Yan, J. Wang, K. Zhang, S. M. Li, Z. P. Xiong, C. Q. Wang, Y. Shiraishi, Y. K. Du and P. Yang, *J. Mater. Chem. A*, 2017, **5**, 15932–15939.

9 S. Wu, Y. Zhu, Y. Huo, Y. Luo, L. Zhang, Y. Wan, B. Nan, L. Cao, Z. Wang, M. Li, M. Yang, H. Cheng and Z. Lu, *Sci. China Mater.*, 2017, **60**, 654–663.

10 Y. Zhou, R. G. Ma, S. L. Candelaria, J. C. Wang, Q. Liu, E. Uchaker, P. X. Li, Y. F. Chen and G. Z. Cao, *J. Power Sources*, 2016, **314**, 39–48.

11 R. G. Ma, Y. Zhou, P. X. Li, Y. F. Chen, J. C. Wang and Q. Liu, *Electrochim. Acta*, 2016, **216**, 347–354.

12 R. G. Ma, B. Y. Xia, Y. Zhou, P. X. Li, Y. F. Chen, Q. Liu and J. C. Wang, *Carbon*, 2016, **102**, 58–65.

13 R. G. Ma, X. D. Ren, B. Y. Xia, Y. Zhou, C. Sun, Q. Liu, J. J. Liu and J. C. Wang, *Nano Res.*, 2016, **9**, 808–819.

14 R. G. Ma, X. D. Ren, B. Y. Xia, Y. Zhou, C. Sun, Q. Liu, J. J. Liu and J. C. Wang, *Nano Res.*, 2017, **10**, 2332–2343.

15 Q. C. Wang, Z. Y. Chen, N. Wu, B. Wang, W. He, Y. P. Lei and Y. D. Wang, *ChemElectroChem*, 2017, **4**, 514–520.

16 Y. P. Lei, Q. Shi, C. Han, B. Wang, N. Wu, H. Wang and Y. D. Wang, *Nano Res.*, 2016, **9**, 2498–2509.

17 C. Q. Shang, M. C. Li, Z. Y. Wang, S. F. Wu and Z. G. Lu, *ChemElectroChem*, 2016, **3**, 1437–1445.

18 R. Li, X. Z. Wang, Y. F. Dong, X. Pan, X. G. Liu, Z. B. Zhao and J. S. Qiu, *Carbon*, 2018, **132**, 580–588.

19 Y. Y. Liang, Y. G. Li, H. L. Wang, J. G. Zhou, J. Wang, T. Regier and H. J. Dai, *Nat. Mater.*, 2011, **10**, 780–786.

20 (*a*) X. Han, G. He, Y. He, J. Zhang, X. Zheng, L. Li, C. Zhong, W. Hu, Y. Deng and T.-Y. Ma, *Adv. Energy Mater.*, 2018, 1702222; (*b*) H. Lee, J. Lim, C. Lee, S. Back, K. An, J. W. Shin, R. Ryoo, Y. Jung and J. Y. Park, *Nat. Commun.*, 2018, **9**, 2235.

21 B. Y. Li, Y. H. Zhang, R. F. Du, L. Liu and X. L. Yu, *Nanotechnology*, 2018, **29**, 8.

22 Q. S. Huang, P. J. Zhou, H. Yang, L. L. Zhu and H. Y. Wu, *Electrochim. Acta*, 2017, **232**, 339–347.

23 S. J. Guo, S. Zhang, L. H. Wu and S. H. Sun, *Angew. Chem., Int. Ed.*, 2012, **51**, 11770–11773.

24 Y. Liu, Y. Liu, S. H.-S. Cheng, S. Yu, B. Nan, H. Bian, K. Md, M. Wang, C. Y. Chung and Z.-G. Lu, *Electrochim. Acta*, 2016, **219**, 560–567.

25 X. Zhang, R. R. Liu, Y. P. Zang, G. Q. Liu, G. Z. Wang, Y. X. Zhang, H. M. Zhang and H. J. Zhao, *Chem. Commun.*, 2016, **52**, 5946–5949.

26 C. D. Bai, S. S. Wei, D. R. Deng, X. D. Lin, M. S. Zheng and Q. F. Dong, *J. Mater. Chem. A*, 2017, **5**, 9533–9536.

27 Z. Zeng, T. Zhang, Y. Y. Liu, W. D. Zhang, Z. Y. Yin, Z. W. Ji and J. J. Wei, *ChemSusChem*, 2018, **11**, 580–588.

28 I. A. Khan, A. Badshah and M. A. Nadeem, *Catal. Commun.*, 2017, **99**, 10–14.

29 H. Kim, Y. Kim, Y. Noh, S. Lee, J. Sung and W. B. Kim, *ChemCatChem*, 2017, **9**, 1503–1510.

30 J. Li, Q. F. Wang, K. Liu, J. B. Jiang, D. Qian, J. H. Li and Z. H. Chen, *Mater. Lett.*, 2017, **186**, 189–192.

31 M. Liu, J. J. Liu, Z. L. Li and F. Wang, *ACS Appl. Mater. Interfaces*, 2018, **10**, 7052–7060.

32 L. Lv, D. Zha, Y. Ruan, Z. Li, X. Ao, J. Zheng, J. Jiang, H. M. Chen, W.-H. Chiang, J. Chen and C. Wang, *ACS Nano*, 2018, **12**, 3042–3051.

33 X. F. Zheng, G. F. Shen, Y. Li, H. N. Duan, X. Y. Yang, S. Z. Huang, H. E. Wang, C. Wang, Z. Deng and B. L. Su, *J. Mater. Chem. A*, 2013, **1**, 1394–1400.

34 V. G. Hadjiev, M. N. Iliev and I. V. Vergilov, *J. Phys. C: Solid State Phys.*, 1988, **21**, L199–L201.

35 (*a*) R. Gao, Z. Y. Li, X. L. Zhang, J. C. Zhang, Z. B. Hu and X. F. Liu, *ACS Catal.*, 2016, **6**, 400–406; (*b*) C. Y. Zhao, Y. Cai, K. L. Yin, H. Z. Li, D. Shen, N. Qin, Z. G. Lu, C. P. Liu and H. E. Wang, *Chem. Eng. J.*, 2018, **350**, 201–208.

36 R. Gao, L. Liu, Z. B. Hu, P. Zhang, X. Z. Cao, B. Y. Wang and X. F. Liu, *J. Mater. Chem. A*, 2015, **3**, 17598–17605.

37 H. E. Wang, X. Zhao, X. C. Li, Z. Y. Wang, C. F. Liu, Z. G. Lu, W. J. Zhang and G. Z. Cao, *J. Mater. Chem. A*, 2017, **5**, 25056–25063.

38 H. K. Wang, X. M. Yang, Q. Z. Wu, Q. B. Zhang, H. X. Chen, H. M. Jing, J. K. Wang, S. B. Mi, A. L. Rogach and C. M. Niu, *ACS Nano*, 2018, **12**, 3406–3416.

39 T. Liu, Y. F. Guo, Y. M. Yan, F. Wang, C. Deng, D. Rooney and K. N. Sun, *Carbon*, 2016, **106**, 84–92.

40 H. E. Wang, X. Zhao, K. L. Yin, Y. Li, L. H. Chen, X. Y. Yang, W. J. Zhang, B. L. Su and G. Z. Cao, *ACS Appl. Mater. Interfaces*, 2017, **9**, 43665–43673.

41 Y. Cai, H. E. Wang, X. Zhao, F. Huang, C. Wang, Z. Deng, Y. Li, G. Z. Cao and B. L. Su, *ACS Appl. Mater. Interfaces*, 2017, **9**, 10652–10663.

42 B. Y. Xia, Y. Yan, N. Li, H. B. Wu, X. W. Lou and X. Wang, *Nat. Energy*, 2016, **1**, 15006.

43 S. Gadipelli, T. T. Zhao, S. A. Shevlin and Z. X. Guo, *Energy Environ. Sci.*, 2016, **9**, 1661–1667.